Available online at www.sciencedirect.com
SCIENCE DIRECT
Journal of Power Sources 156 (2006) 434–447
JOURNAL OF POWER SOURCES
www.elsevier.com/locate/jpowsour

Gas-phase reactions of methane and natural-gas with air and steam in non-catalytic regions of a solid-oxide fuel cell

Gaurav K. Gupta[a], Ethan S. Hecht[b], Huayang Zhu[b], Anthony M. Dean[a,*], Robert J. Kee[b]

[a] *Chemical Engineering Department, Colorado School of Mines, 1613 Illinois Street, Golden, CO 80401, USA*
[b] *Engineering Division, Colorado School of Mines, 1613 Illinois Street, Golden, CO 80401, USA*

Received 10 May 2005; received in revised form 7 June 2005; accepted 9 June 2005
Available online 22 July 2005

Abstract

This paper uses a large elementary reaction mechanism to study the homogeneous chemistry of methane and natural-gas mixed with air and steam. Temperatures and residence times are chosen to represent SOFC operating conditions, including within feed lines that may be at elevated temperature but without any electrochemical or catalytic interactions. Mole fractions of six major species (CH_4, O_2, H_2O, H_2, CO, and CO_2) are presented as contour maps as functions of temperature, residence time, and initial fuel mixture compositions. In addition, deposit propensity is predicted by the sum of mole fractions of all species containing five or more carbon atoms, designated as C^{5+}. Comparison with chemical equilibrium predictions shows that the homogeneous reactions are far from equilibrium. These results indicate that the composition of the fuel mixture entering the active SOFC region might be significantly different from that originally entering the fuel cell.

Keywords: Deposits; Gas-phase kinetics; Methane; Natural gas; Steam; Air

1. Introduction

In principle solid-oxide fuel cells (SOFCs) can operate directly with hydrocarbon fuels, although in practice measures must be taken to inhibit carbon-deposit formation [1–11]. It is often desirable to premix steam or air with the hydrocarbon to counteract deposit formation and possibly to assist with thermal management [11–13]. Depending on system design, inlet fuel mixtures can be exposed to high temperatures within flow-distribution networks before entering the active regions of the fuel cell. Although gas-phase chemistry continues within the cell, the homogeneous chemistry in that region may be strongly influenced by electrochemistry and catalytic heterogeneous chemistry (both of which are outside the scope of this paper).

This paper uses a detailed reaction mechanism to model the purely homogeneous pyrolysis and oxidation chemistry associated with initial mixtures of methane or natural-gas with steam and air. It considers temperatures ranging from 600 to 900 °C and residence times ranging from 0.1 to 1000 s. We distinguish between methane and natural-gas to explicitly account for expected increased chemical reactivity of the higher hydrocarbons commonly found in natural-gas. In our calculations we assume that the fuel is free from the impurities (e.g., sulphur). Homogeneous chemistry plays two potentially important roles. First it acts to convert the initial hydrocarbon fuel into H_2, CO, H_2O and other compounds. Thus the "fuel" that enters the active regions of the fuel cell may not be the initial fuel (e.g., natural-gas) supplied to the system. Second, molecular-weight–growth via homogeneous chemistry can ultimately lead to polyaromatic hydrocarbon deposits [14].

Results are presented in the form of contour maps showing species mole fractions as functions of temperature, residence time, and initial fuel mixture composition. Deposit propensity is predicted by the sum of mole fractions of all species containing five or more carbon atoms, designated as C^{5+}. Increased temperature causes increased reaction. Generally speaking, natural-gas is always more reactive than methane alone. Fuel–air mixtures are significantly more reactive than fuel–steam mixtures. By comparing with chemical-

* Corresponding author. Tel.: +1 303 273 3643; fax: +1 303 273 3730.
E-mail address: amdean@mines.edu (A.M. Dean).

0378-7753/$ – see front matter © 2005 Elsevier B.V. All rights reserved.
doi:10.1016/j.jpowsour.2005.06.003

equilibrium predictions, it is evident that kinetic process controls the homogeneous chemistry under conditions relevant to SOFC operation.

2. Model description

The model is based on the constant-temperature-and-pressure species continuity equation [15]

$$\frac{dY_k}{dt} = \frac{\dot{\omega}_k W_k}{\rho} \quad (1)$$

where the independent variable is the time t and the dependent variables are the mass fractions Y_k. The molecular weights are W_k and the mass density ρ is computed using a perfect-gas equation of state. The species molar production rates $\dot{\omega}_k$ are determined from the elementary reaction mechanism. As discussed below, the mechanism involves about 350 species and 3450 reactions.[1] All reactions are reversible, with the reverse rate coefficients computed from the temperature-dependent equilibrium constants.

Mathematically the model is an ordinary-differential-equation initial-value problem, which is solved computationally using DVODE [16]. The CHEMKIN software is used to evaluate chemical production rates from the reaction mechanism [17]. Although a constant-temperature constraint is imposed here, one could easily make other choices. For example, one could impose a temperature–time profile, such as might be derived from knowledge of feed-line temperatures. One could also solve the thermal-energy equation to determine temperature variations associated with the reaction kinetics. By simply specifying a temperature the results can be generalized into sets of contour maps without specific regard to a particular fuel-cell system design.

The reaction mechanism used here is an extension of one used earlier to describe butane pyrolysis [14]. It incorporates oxidation and pyrolysis kinetics for hydrocarbons up to C_6. Additionally it includes the molecular-weight–growth reactions for polyaromatic hydrocarbon (PAH) formation via the hydrogen-abstraction–acetylene-addition mechanism of Frenklach and Warnatz [18]. This earlier mechanism is referred to as the "Sheng–Dean" mechanism.

The mechanism in the current work is modified from the Sheng–Dean mechanism as follows:

1. The rate coefficients for hydrogen-abstraction reactions from cyclopentadiene were updated using recent results for the standard heat of formation of the cyclopentadienyl radical [19]. The new value is 261.2 kJ mol^{-1}, some 21 kJ mol^{-1} higher than the previous value.
2. A substantial number of pressure-dependent reactions, including dissociation of stable hydrocarbons, beta-scission of hydrocarbon and oxygenated radicals, and radical recombination reactions were updated [20].
3. The methane-dissociation reaction rate ($CH_4 \rightleftharpoons H + CH_3$) was lowered by a factor of 4.
4. The rate for hydrogen abstraction from ethane by methyl ($C_2H_6 + CH_3 \rightleftharpoons C_2H_5 + CH_4$) was updated to the value reported in the GRI-3.0 mechanism [21].

[1] The mechanism and the associated thermodynamic database are available upon request.

3. Mechanism validation

There is limited data published for methane oxidation or pyrolysis in the SOFC operating temperature regime. These data include methane pyrolysis near 1000 K [22,23] and simulated natural-gas oxidation between 1100 and 1200 K [24]. As discussed in the following sections, the current mechanism is better able to represent the data than the earlier Sheng–Dean mechanism.

3.1. Methane pyrolysis

Back and coworkers [22,23] measured the production of C_2H_6, C_2H_2, H_2, C_2H_4, C_3H_6, and C_3H_4 at very low levels of methane conversion at 1038 K and 0.58 atm. An interesting feature of the pyrolysis data is the increase in rate with time (Fig. 1). This behavior is especially evident for ethane, where the mole fraction is essentially constant between 500 and 1500 s before undergoing a significant increase beyond 1500 s. Fig. 1 shows that the Sheng–Dean mechanism agrees well with the ethane production at shorter times. However the current mechanism represents the ethane data much better at longer times. Fig. 1 shows that the current mechanism does a reasonable job of representing the transient behavior of all measured species.

3.2. Methane oxidation

El Bakali et al. [24] used steady-state jet-stirred reactor experiments to study the reaction of methane/ethane/oxygen mixtures at various temperatures and atmospheric pressure. The initial composition was 0.73% CH_4, 0.073% C_2H_6, 1.14% O_2 with the balance nitrogen. The relatively small ethane addition was used to simulate natural-gas. Mole fractions of CH_4, C_2H_6, C_2H_4, C_2H_2 and O_2 were measured at a residence time of 0.14 s. Only the lowest temperature data (1100–1200 K) is used here, because it is closest to the SOFC operating range.

Fig. 2 illustrates a comparison between the model predictions and measured mole fractions. As with methane pyrolysis, the current mechanism represents the data reasonably well. However the model does predict a somewhat stronger temperature dependence than is observed. These comparisons suggest that the current mechanism should provide reasonable predictions of gas-phase kinetics under SOFC operating conditions.

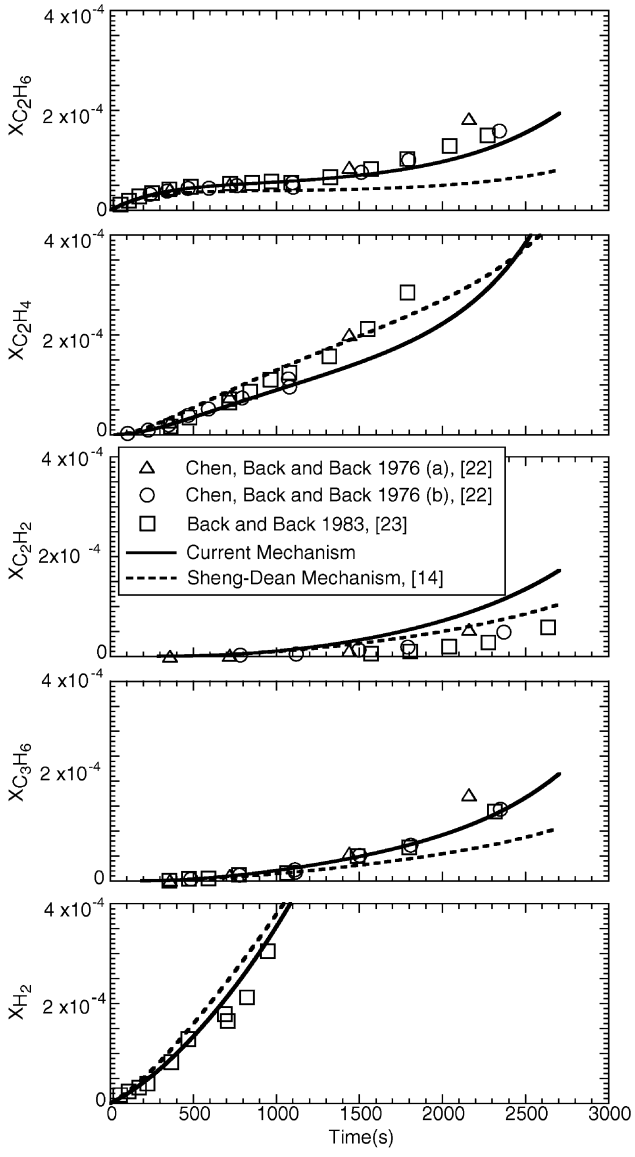

Fig. 1. Comparison of the model predictions for mole fractions of C_2H_6, C_2H_4, C_2H_2, C_3H_6, and H_2 to various CH_4 pyrolysis experiments at 1038 K and 0.58 atm. [22,23]. Experimental data (a) refers to the tabulated data reported in [22], (b) refers to data extracted from Fig. 4 of the same work.

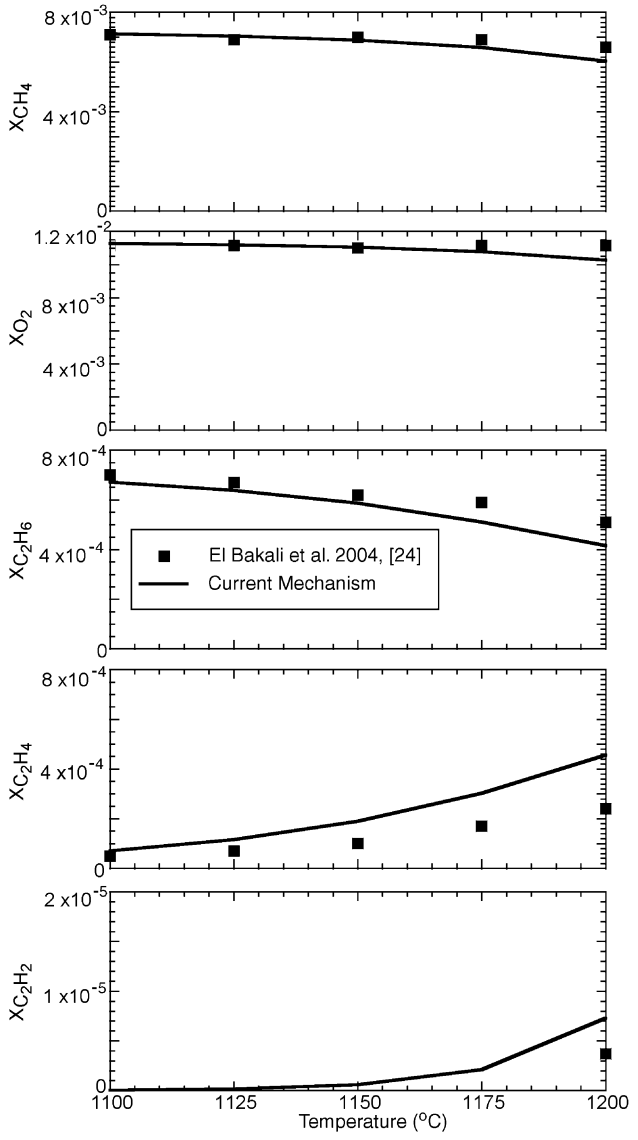

Fig. 2. Comparison of the model predictions for mole fractions of CH_4, O_2, C_2H_6, C_2H_4, and C_2H_2 to the CH_4 oxidation experiments of El Bakali et al. [24] done at 1 atm.

4. Results and discussion

The modeling here is motivated by the fact that hydrocarbon fuels are often mixed with steam or air prior to introduction into the SOFC. This strategy can improve system performance, including the inhibition of deposit formation. The results in this paper are based on modeling the transient homogeneous kinetics of methane and natural-gas reacting with air and steam. The simulations are isothermal and isobaric, with temperatures ranging from 600 to 900 °C and pressure fixed at 1 atm. Results are reported for residence times ranging from 0.1 to 1000 s. For the fuel–steam mixtures the initial fuel mole fractions range between 0 and 1. For the fuel–air mixtures the initial fuel mole fractions range between 0.2 and 1. An initial fuel mole fraction of 0.2 corresponds approximately to an equivalence ratio of $\phi = 2.1$. Mixtures with methane mole fractions lower than 0.2 would be sufficiently close to combustion conditions that the fuel would simply burn and thus be of little practical interest for SOFC operation. Even though there is little practical value to SOFC fuels that are primarily steam, results for the entire range of initial fuel–steam mole fractions are presented.

Although methane is the dominant constituent of natural-gas, it is well known that the non-methane constituents of natural-gas can cause significant differences in the reaction chemistry. For purposes of this paper, we assign natural-gas, designated here as CH_4^*, the composition given in Table 1, which is representative of pipeline natural-gas.

Table 1
Composition of natural-gas (CH_4^*) used in the calculations

Species	Molar (%)
CH_4	94.5
C_2H_6	2.5
C_3H_8	0.3
n-C_4H_{10}	0.05
Iso-C_4H_{10}	0.05
N_2	1.7
CO_2	0.9

The results are presented as contour maps showing mole fractions of the six major species as a function of residence time and the initial fuel mixture composition at a fixed temperature. The propensity to form polyaromatic deposits is characterized by the sum of mole fractions of all product species that contain five or more carbon atoms, designated here as C_{5+}.

In studying butane pyrolysis, Sheng and Dean found that the onset of deposit formation could be correlated with predicted levels of C_{5+} [14]. Many of these high-molecular-weight species are cyclic unsaturated compounds that are precursors of polynuclear aromatic hydrocarbons (PAH). Moreover, forming the first aromatic ring is generally considered to be the rate-limiting step in the formation of PAHs. Flowing butane in quartz tubes, Sheng and Dean reported deposit formation at a nominal temperature of 700 °C and residence time of 5 s. Under these conditions, they predicted that the mole fraction of C_{5+} was approximately 10^{-3}, suggesting this value as an approximate threshold for deposit formation.

4.1. Fuel–air mixtures

At 600 °C with methane as the fuel, the top two panels of Fig. 3 (CH_4 and O_2) show that below a residence time of 1 s very little reaction occurs, except at low mole fractions of methane. Beyond 1 s the mole fractions of both CH_4 and O_2 start to decrease. By 10 s nearly all the oxygen is consumed over the entire range of mixtures, producing H_2O, H_2, CO and small amounts of CO_2 (panels 3–6 of Fig. 3). Note that once oxygen is completely reacted, the contours become nearly flat (i.e., independent of time). Fig. 3 shows that the H_2O and CO_2 mole fractions increase monotonically as the initial mole fraction of CH_4 decreases and the mixture becomes more oxidizing. However H_2 and CO mole fractions peak at intermediate levels of initial CH_4 mole fractions. At lower initial CH_4 mole fractions, H_2 and CO are oxidized to H_2O and CO_2. As the initial methane mole fraction decreases toward 0.2 the production rate of all product species is decreased, likely caused by a lower radical-production rate at the lower methane concentrations.

The bottom panel in Fig. 3 shows predictions for C_{5+} levels. With such low levels predicted here, there is little likelihood of deposit formation from gas-phase reactions for any fuel–air mixtures. However, it is interesting to note the increased tendency toward molecular-weight–growth at in-

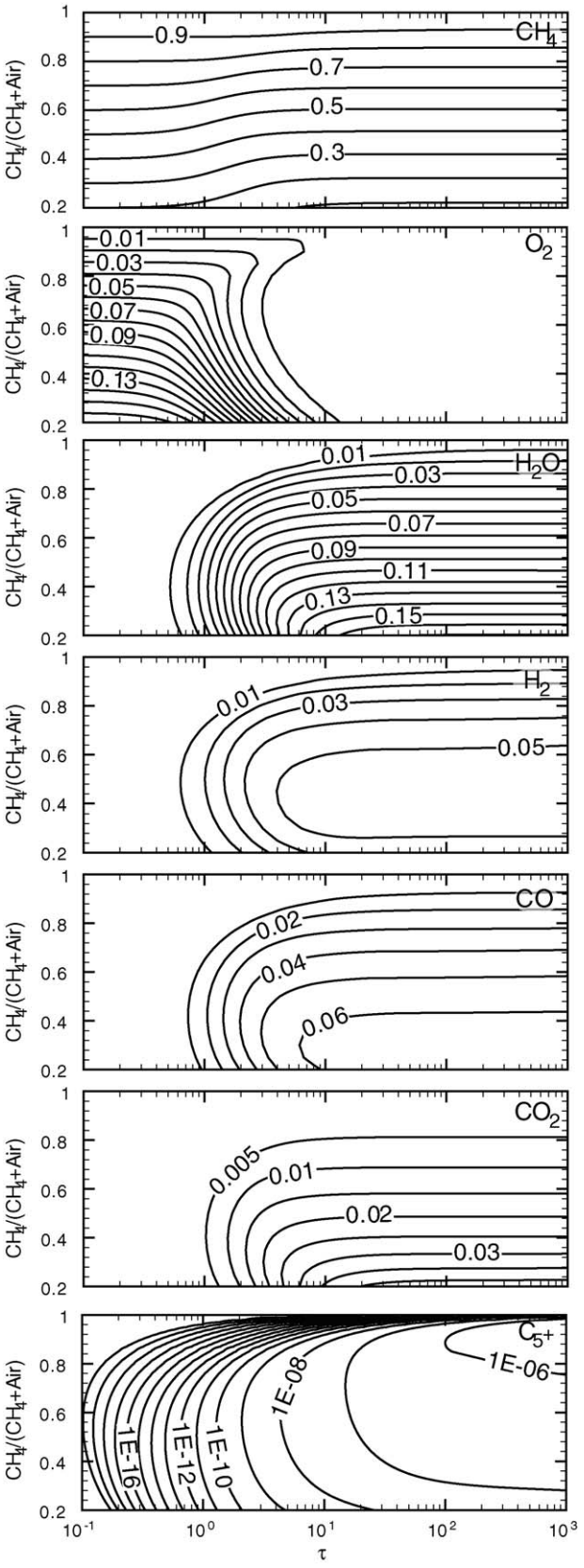

Fig. 3. Predicted mole fractions as a function of residence time and initial extent of mixing for methane–air mixtures at 600 °C.

termediate initial methane mole fractions. The formation reactions are slower at low air levels due to the intrinsic stability of methane. The radical pool is insufficient to drive the molecular-weight–growth kinetics. At high air levels the molecular-weight–growth reactions are inhibited by the lower concentrations of methane.

Fig. 4 summarizes the natural-gas–air predictions at 600 °C. Generally speaking the kinetics are slightly faster than those for methane. In the case of natural-gas, oxygen is depleted faster at low mole fractions of O_2. This is due to the fact that the higher hydrocarbons present in the natural-gas are more reactive than methane. The product distribution is similar to the methane case, but generally reactions start slightly earlier. The most significant difference is the predicted production of C_{5+}, with substantially more growth predicted for the natural-gas case. Such a result is anticipated because the natural gas contains more-reactive hydrocarbons. Moreover, the natural-gas has a "head start" toward molecular-weight–growth due to the initially present higher hydrocarbons. Note however that the overall level of molecular-weight–growth is still predicted to be very low. Assuming a threshold of $C^{5+} > 0.001$ for deposit formation, the likelihood for PAH formation at 600 °C is still quite low.

Figs. 5 and 6 show predictions at 700 °C. For methane–air mixtures (Fig. 5), there is relatively little effect of the increased temperature at high initial CH_4 mole fractions. This may be seen by comparing the O_2 contours with the 600 °C case. However at lower initial methane mole fractions reactions begin earlier than at 600 °C, which is evident from comparison of the major-product profiles. As at 600 °C, once oxygen is completely reacted, the profiles of the major products become nearly constant in time. The major differences at 700 °C as compared to 600 °C are as follows:

1. H_2 peaks at approximately 5% for both temperatures, but at 700 °C the peak occurs earlier in time and the high-H_2 region is larger.
2. At the higher temperature, CO continues to increase as the methane mole fraction decreases.
3. The mole fraction of C_{5+} is larger by almost two orders of magnitude.

Fig. 6 shows predictions for the natural-gas–air case at 700 °C. As at 600 °C, the results show natural-gas to be more reactive than methane. The relative differences at 700 °C between the two fuels are similar to those predicted at 600 °C. Relative to methane, natural-gas leads to a substantial increase in the predicted C_{5+} levels.

The predictions at 800 °C are shown in Figs. 7 and 8. The methane–air results (Fig. 7) indicate that oxygen is depleted even earlier at higher temperature, generally within a few seconds residence time. Although the species distributions are similar to the 700 °C cases, the time dependence is now significantly altered. This is most evident for H_2, where the mole fraction sharply increases at long times and low levels of air mole fraction, long after oxygen has completely

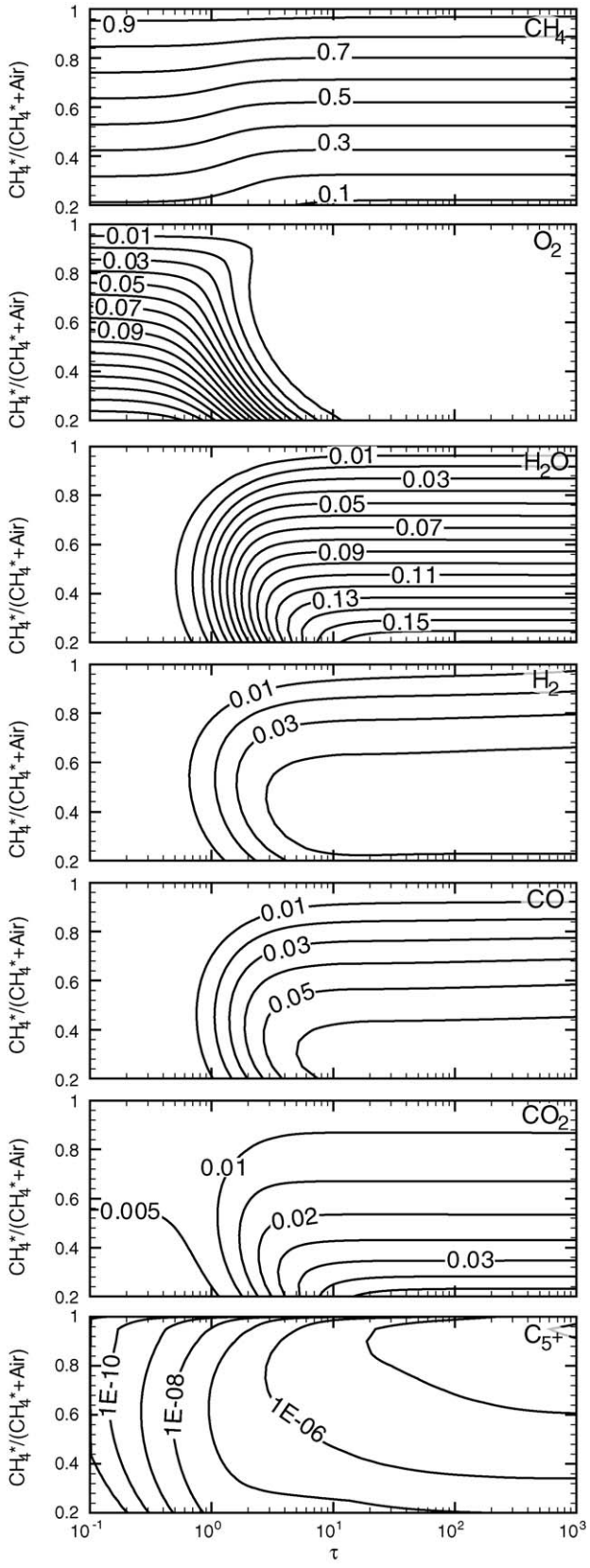

Fig. 4. Predicted mole fractions as a function of residence time and initial extent of mixing for natural-gas (CH_4^*)–air mixtures at 600 °C.

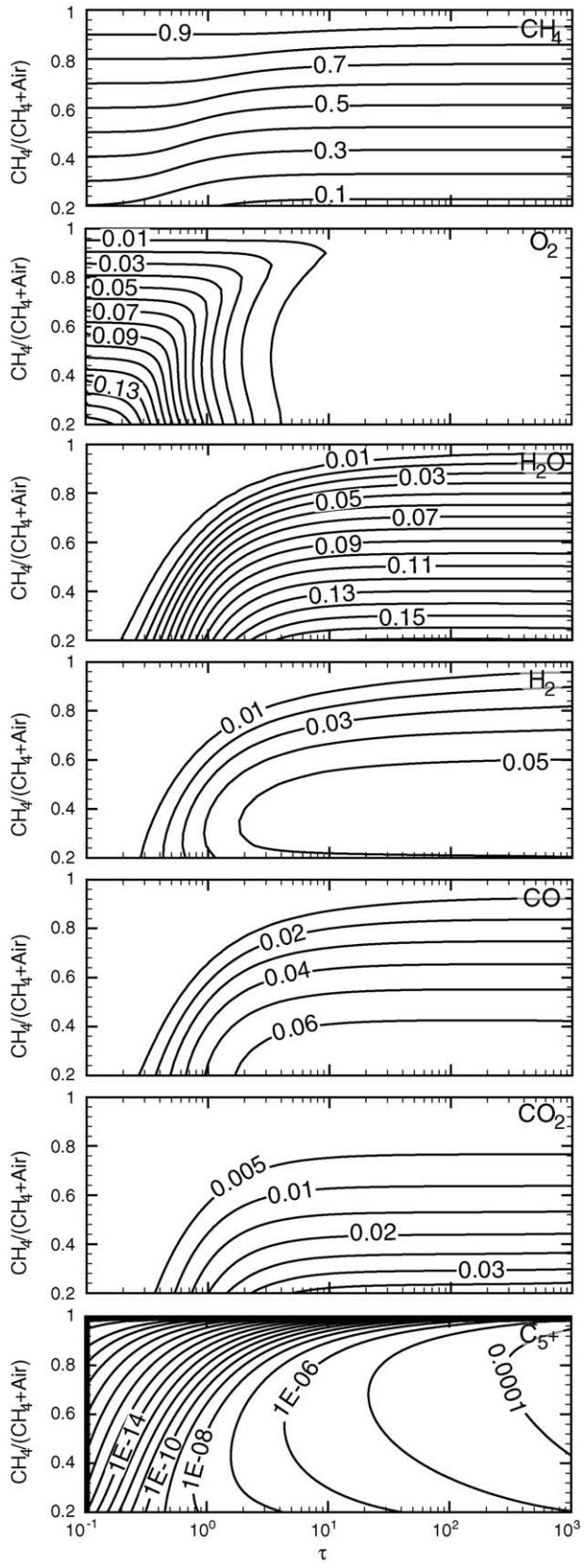

Fig. 5. Predicted mole fractions as a function of residence time and initial extent of mixing for methane–air mixtures at 700 °C.

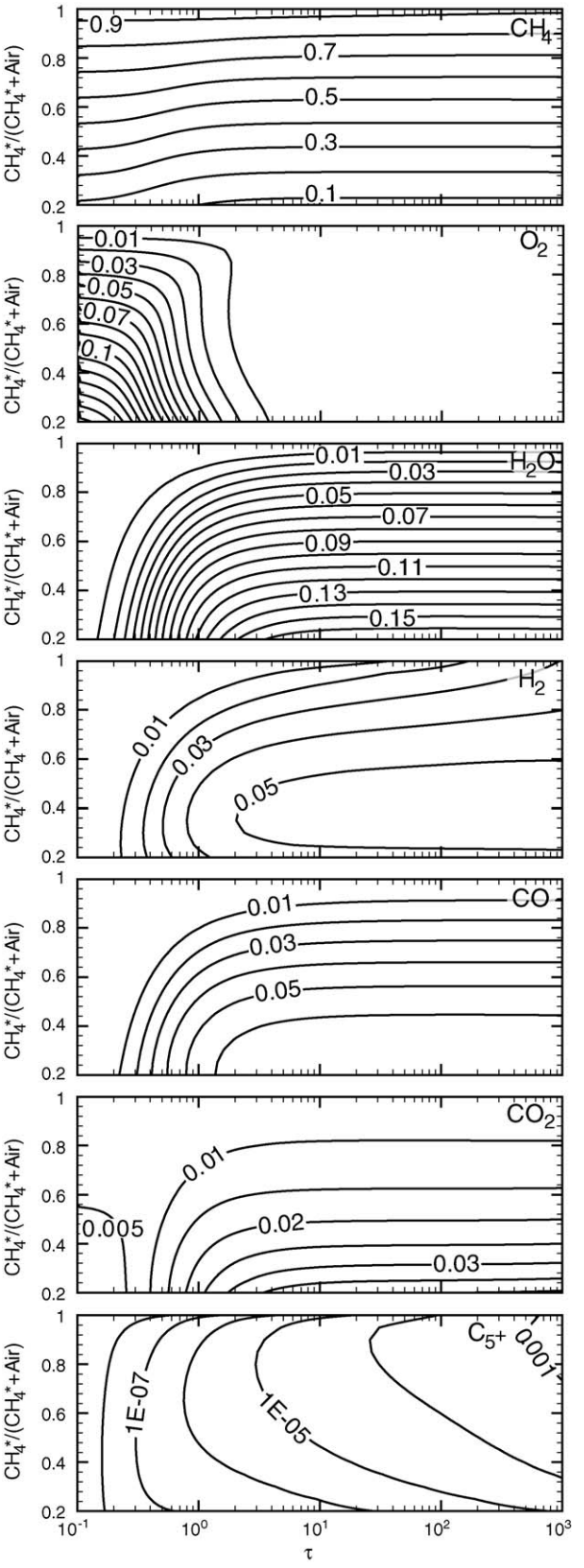

Fig. 6. Predicted mole fractions as a function of residence time and initial extent of mixing for natural-gas (CH_4^*)–air mixtures at 700 °C.

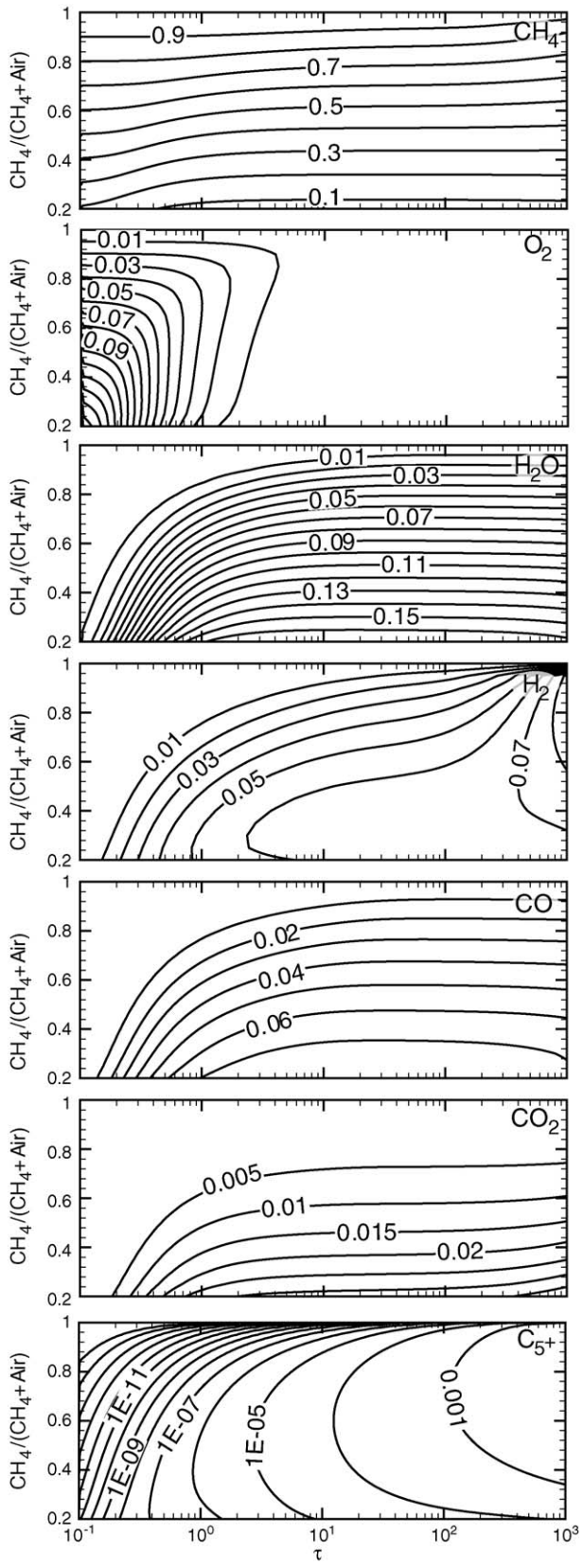

Fig. 7. Predicted mole fractions as a function of residence time and initial extent of mixing for methane–air mixtures at 800 °C.

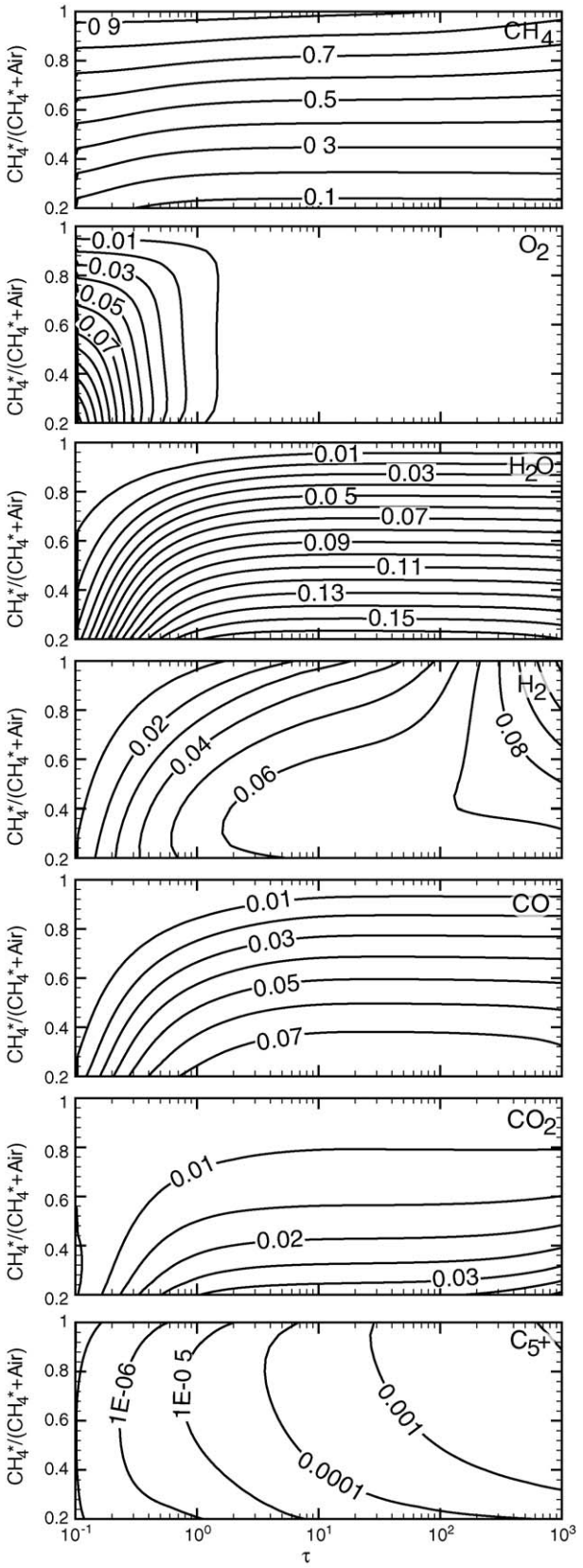

Fig. 8. Predicted mole fractions as a function of residence time and initial extent of mixing for natural-gas (CH_4^*)–air mixtures at 800 °C.

reacted. The increase in H_2 is accompanied by a decrease in CH_4. These changes result from the fact that the system begins to behave autocatalytically, similar to the pyrolysis results shown in Fig. 1. As illustrated in Fig. 7, this increased H_2 production rate begins around 100 s, which is somewhat earlier than observed in the pyrolysis experiments (Fig. 1). However, one expects this time shift since the calculations are at slightly higher temperatures and pressures.

At 800 °C continued increases in C_{5+} levels are predicted. The mole fraction is now higher by about an order of magnitude than predicted at 700 °C at any particular residence time or mixture composition. As seen at lower temperatures, Fig. 8 shows that the natural-gas is more reactive than methane. With natural-gas, products appear at slightly earlier times and the deposit likelihood increases.

The predictions at 900 °C (Figs. 9 and 10) indicate that substantial gas-phase chemistry occurs long after oxygen is depleted. The concentration of H_2 increases dramatically at long residence times and low air mole fractions as methane continues to react. The mole fraction of CO is generally much higher than that of CO_2. The higher temperature significantly increases the tendency to form deposits. The predictions with natural-gas as the fuel are quite similar to those for methane. The temperature is now sufficiently high that the reactivity difference between methane and the higher hydrocarbons is not so pronounced.

4.2. Fuel–steam mixtures

The fuel–steam mixtures show relatively little homogeneous reactivity, even at the long residence times. Even at 800 °C for the methane case, the top two panels of Fig. 11 (CH_4 and H_2O) indicate almost no reaction. The natural-gas mixtures are more reactive. As shown in Fig. 12 some H_2 is produced, especially at low initial levels of H_2O. The natural-gas mixtures are also more likely to produce deposits at long residence times over a large range of mixture compositions.

Figs. 13 and 14 show that reactivity at 900 °C increases markedly, especially at long residence times. H_2 is the dominant product, and steam becomes a reactant. Note that the predicted hydrogen levels are comparable to those predicted for the air case at long times and low air levels. At 900 °C even the methane–steam system can experience substantial gas-phase molecular-weight–growth. Nevertheless, even at 900 °C, there is virtually no reaction at residence times below 10 s for the methane mixtures. However, natural-gas mixtures are much more reactive, with substantial H_2 production predicted at residence times below 1 s. As expected for natural-gas, the likelihood of deposit formation is generally much larger than for pure methane.

At 900 °C, long times, and low levels of H_2O mole fraction there is an increase in H_2 accompanied by a decrease in CH_4. Similar behavior was observed in the methane and natural-gas–air mixtures. These changes are caused by the system beginning to behave autocatalytically, similar

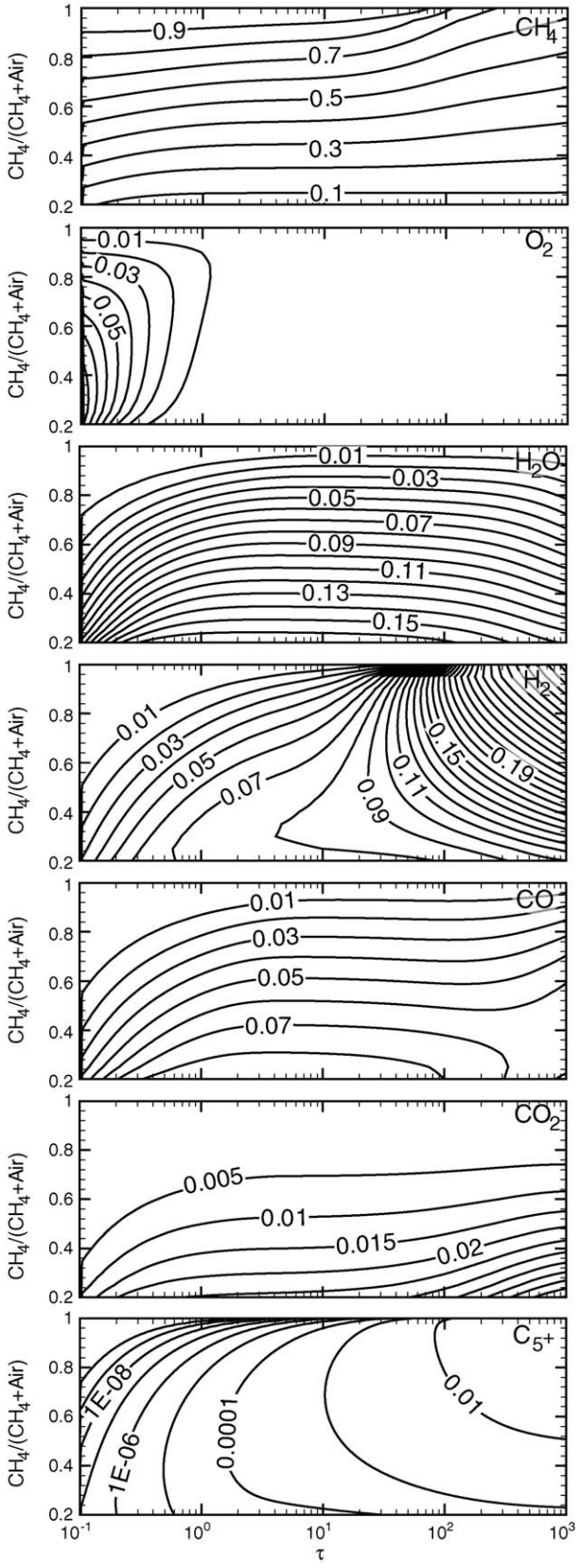

Fig. 9. Predicted mole fractions as a function of residence time and initial extent of mixing for methane–air mixtures at 900 °C.

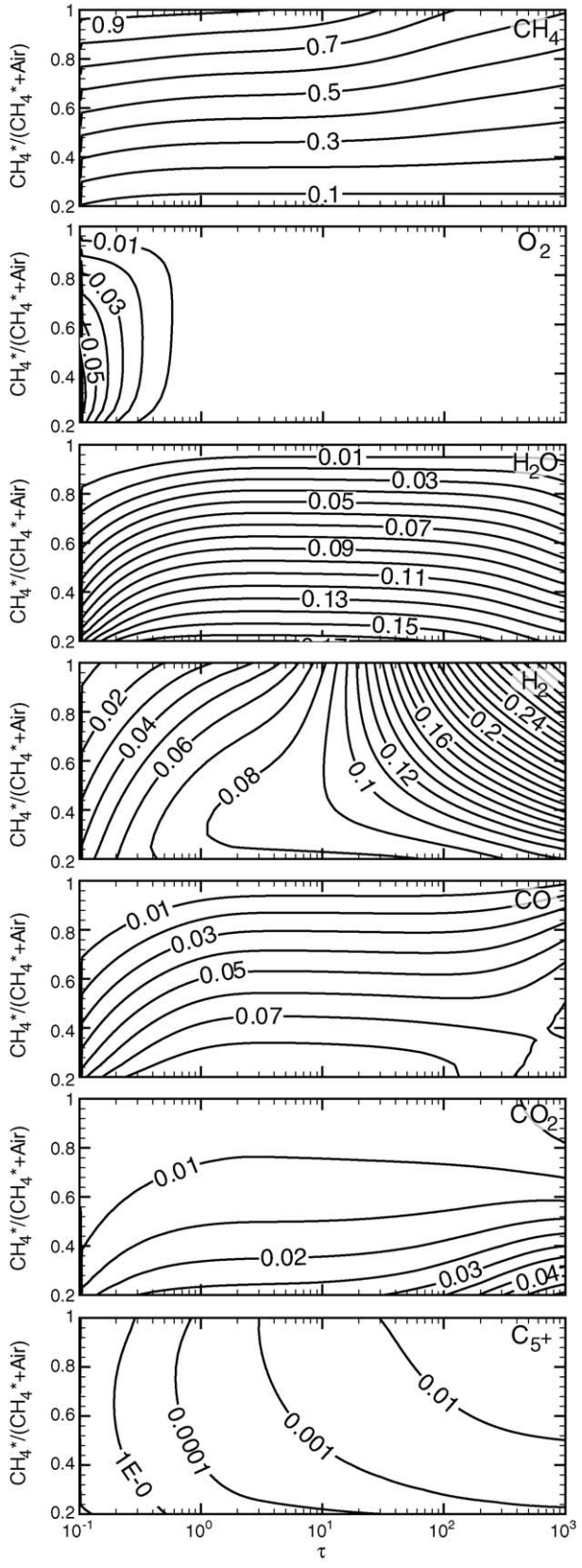

Fig. 10. Predicted mole fractions as a function of residence time and initial extent of mixing for natural-gas (CH_4^*)–air mixtures at 900 °C.

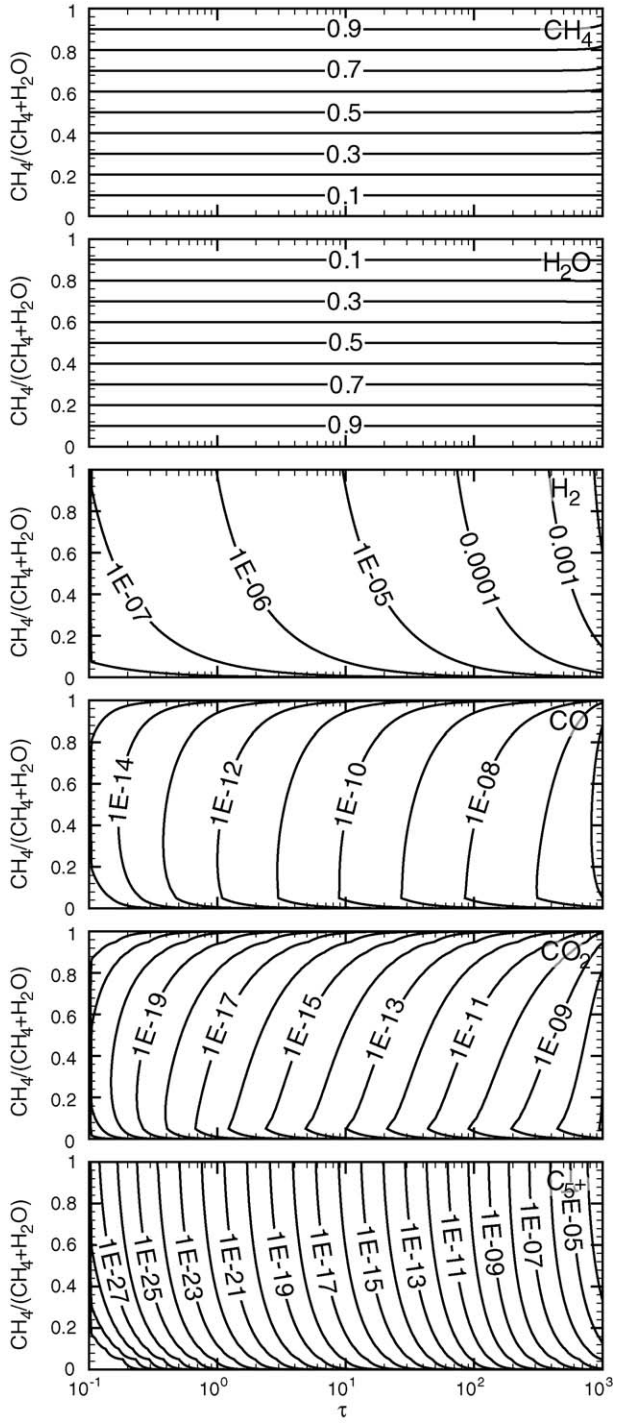

Fig. 11. Predicted mole fractions as a function of residence time and initial extent of mixing for methane–steam mixtures at 800 °C.

to the pyrolysis results in Fig. 1. Under these conditions, pyrolysis causes increased production of H_2 and higher hydrocarbons.

To explore the role of H_2O, the predicted profiles of CH_4 and H_2 for 80% natural-gas and 20% H_2O mixture are compared to those where H_2O is replaced with N_2. Fig. 15 shows that the CH_4 conversion and H_2 production is virtually iden-

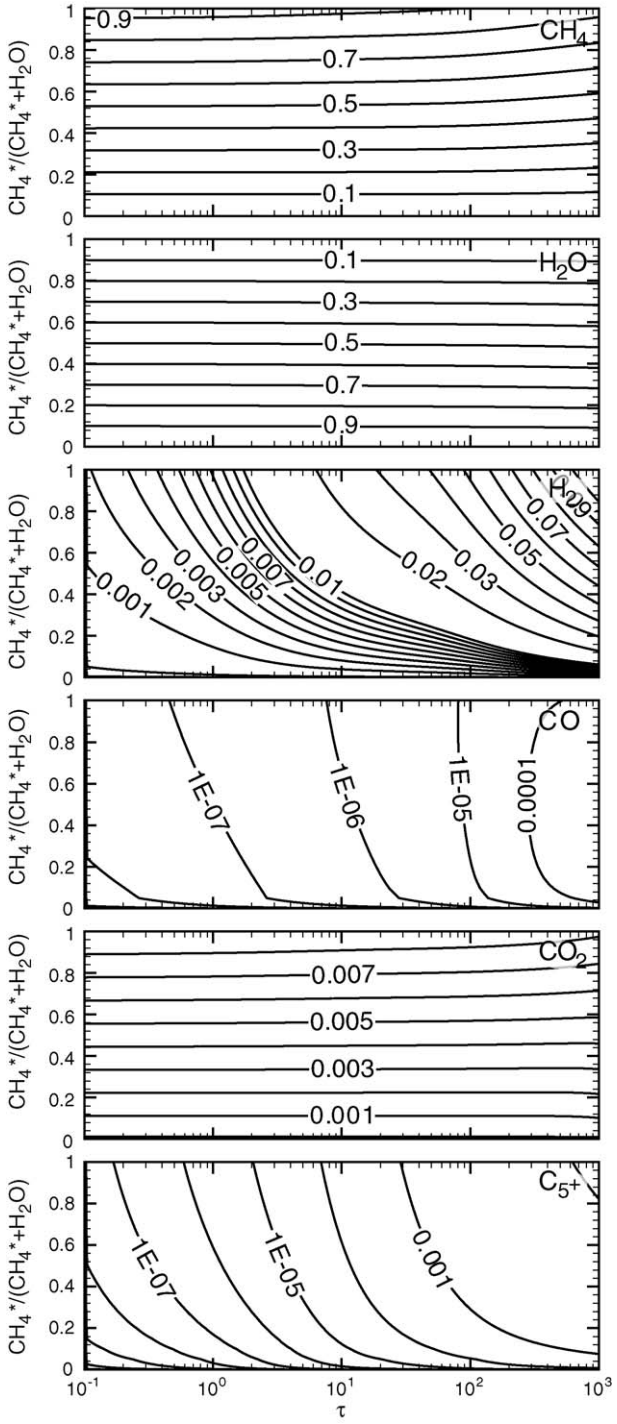

Fig. 12. Predicted mole fractions as a function of residence time and initial extent of mixing for natural-gas (CH_4^*)–steam mixtures at 800 °C.

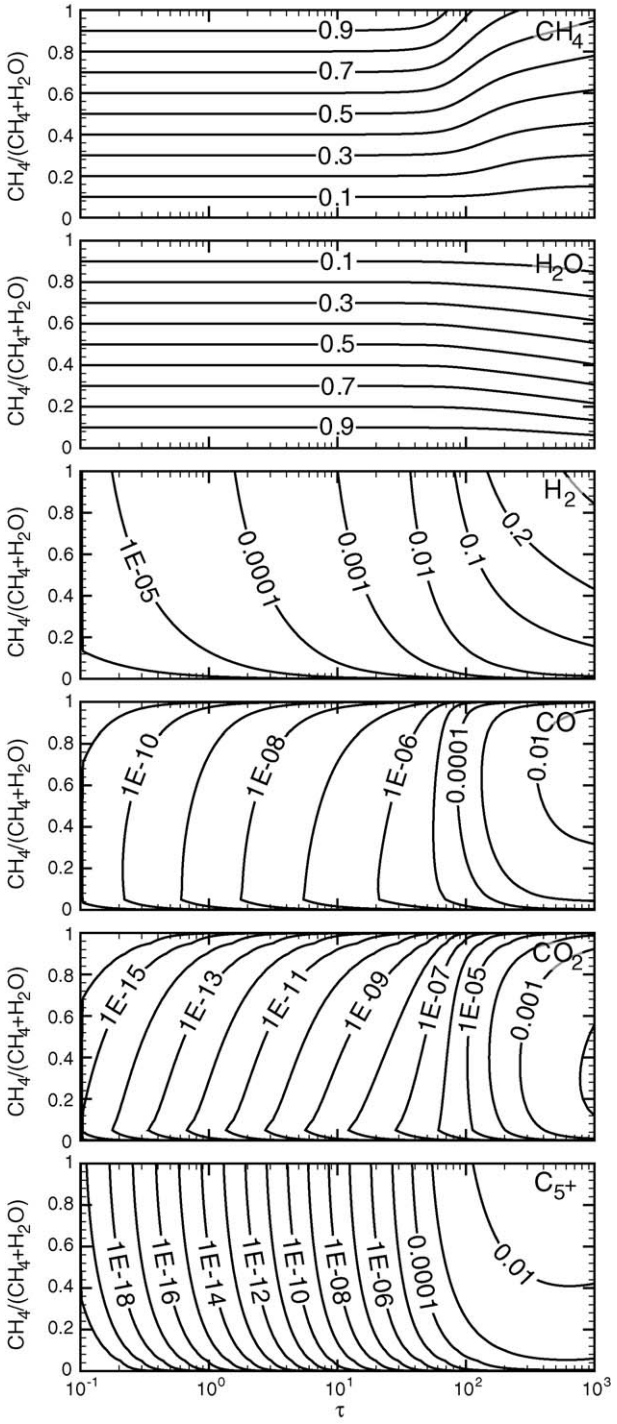

Fig. 13. Predicted mole fractions as a function of residence time and initial extent of mixing for methane–steam mixtures at 900 °C.

tical in the two cases, suggesting that H_2O has little effect on the pyrolysis reactions under these conditions.

At 900 °C, H_2O is responsible for producing small levels of CO and CO_2 as seen in Figs. 13 and 14. The relatively slow endothermic reactions of H_2O with CH_3 and H radicals provides a source of OH via the following reactions:

$$CH_3 + H_2O \rightleftharpoons CH_4 + OH \quad (2)$$

$$H + H_2O \rightleftharpoons H_2 + OH \quad (3)$$

The OH can in turn participate in the following chain reactions to produce CO and CO_2:

$$CH_3 + OH \rightleftharpoons CH_3OH \quad (4)$$

$$CH_3OH + H \rightleftharpoons CH_2OH + H_2 \quad (5)$$

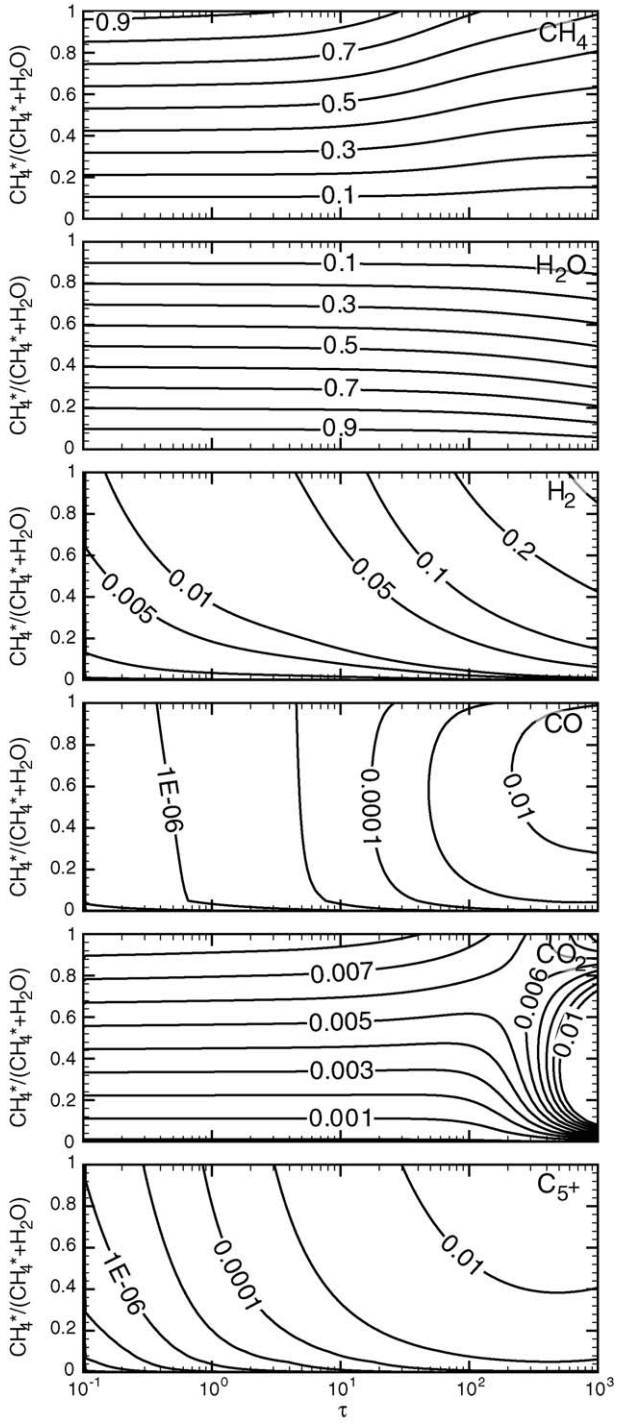

Fig. 14. Predicted mole fractions as a function of residence time and initial extent of mixing for natural-gas (CH_4^*)–steam mixtures at 900 °C.

$$CH_3OH + CH_3 \rightleftharpoons CH_2OH + CH_4 \quad (6)$$

$$CH_2OH \rightleftharpoons CH_2O + H \quad (7)$$

$$CH_2O + H \rightleftharpoons HCO + H_2 \quad (8)$$

$$HCO \rightleftharpoons H + CO \quad (9)$$

$$CO + OH \rightleftharpoons CO_2 + H \quad (10)$$

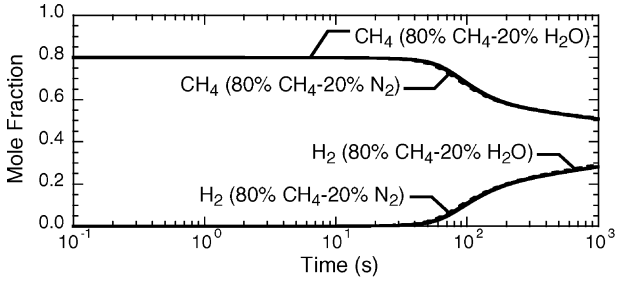

Fig. 15. Comparison of CH_4 and H_2 histories for an 80–20 mixture of natural-gas (CH_4^*) and H_2O and an 80–20 mixture of natural-gas and N_2 at 900 °C.

The radical concentrations, especially CH_3, are lower for the steam case than for the air case. Thus these reactions become important only at a higher temperatures, despite the fact that H_2O concentration is higher.

4.3. Kinetics versus equilibrium

In the fuel–air cases, many of the contour plots show product mole fractions that are independent of time once oxygen is depleted. It is interesting to know if this steady-state behavior is the result of chemical equilibrium or not. Thus direct comparisons are made between the kinetics predictions and the local chemical equilibrium. The constrained temperature–pressure equilibrium conditions are computed using CHEMKIN [17].

Consider cases for natural-gas–air and natural-gas–H_2O mixtures with the natural-gas mole fractions equal to 0.5. Figs. 16 and 17 compare kinetic predictions at residence times of 1000 s and at various temperatures to the equilibrium predictions. It is clear that these systems are far from equilibrated.

Fig. 16 shows that for the natural-gas–air mixture the largest deviations are at the highest temperature where the kinetics are fastest. The gas-phase kinetics leads to over-oxidation of the fuel, with much higher mole fractions of CO_2 and H_2O than expected at equilibrium. The eventual approach toward equilibrium is substantially inhibited since the gas-phase kinetics of reactions of either H_2O or CO_2 with H atoms (e.g., reaction (3) and reaction (10) in the reverse direction) with the hydrocarbon species are very slow, primarily due to the fact that these reactions are endothermic with correspondingly high activation energies. From Fig. 17 it can be seen that for natural-gas–H_2O mixture, there are differences between equilibrium and kinetic predictions over the entire temperature range. The gas-phase kinetics are very slow, leading to much lower mole fractions of CO and H_2 than expected at equilibrium.

In addition to major species, the equilibrium C_{5+} levels are also predicted. Graphite is not included in the equilibrium calculations since it is unlikely to be formed homogeneously on any reasonable timescale. Fig. 18 is a map that shows the regions where the equilibrium C_{5+} is above and below a mole fraction of 10^{-3}. These results suggest significant

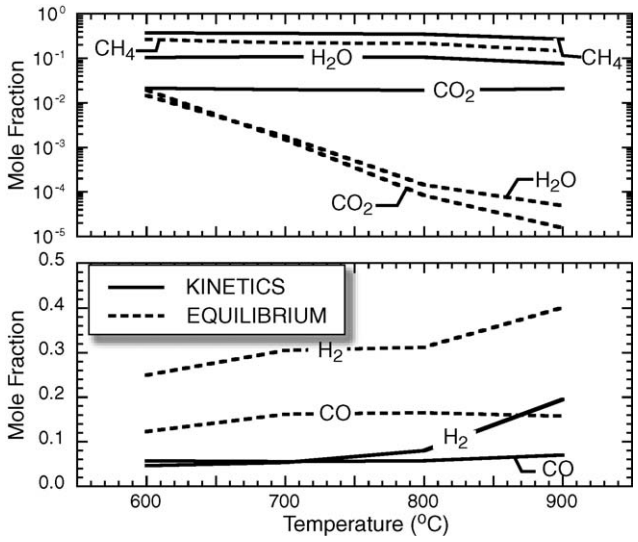

Fig. 16. Comparison of kinetic predictions for a 50–50 mix of natural-gas (CH_4^*) and air at 1000 s to the equilibrium calculations as a function of temperature.

composition and temperature dependencies. At 600 °C, the air mole fraction would need to be at least 0.17 to avoid deposits. As the temperature increases, more air is needed to avoid deposits. By 900 °C nearly 55% air is needed to avoid deposits at equilibrium.

It is interesting to compare the equilibrium predictions with the kinetic predictions of C_{5+}. At 600 °C (Fig. 4) predicted C_{5+} values from the kinetics are significantly lower than 10^{-3} for all conditions, whereas equilibrium indicates that if CH_4 mole fraction is above 0.83 the amount of C_{5+} is greater than 10^{-3}.

At 700 °C, equilibrium predicts that C_{5+} exceeds 10^{-3} at initial natural-gas mole fractions above about 0.74. The

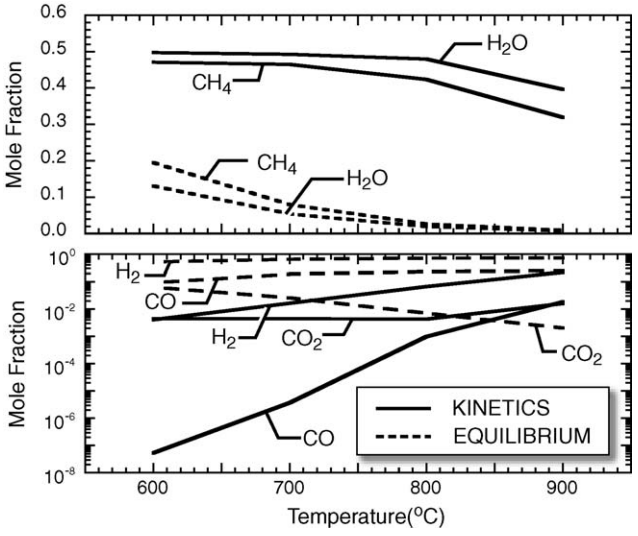

Fig. 17. Comparison of kinetic predictions for a 50–50 mix of natural-gas (CH_4^*) and steam at 1000 s to the equilibrium calculations as a function of temperature.

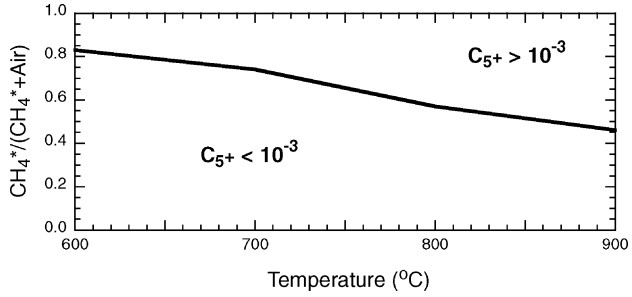

Fig. 18. Predictions of the natural-gas (CH_4^*) mole fraction (in natural-gas–air mixtures) at which the equilibrium C_{5+} exceeds 10^{-3} as a function of temperature.

kinetic predictions at 700 °C also indicate that at very long residence times the C_{5+} exceeds 10^{-3} for natural-gas mole fractions greater than approximately 0.7. However, from the shape of the contours one expects that at residence times greater than 1000 s the predicted C_{5+} levels exceed 10^{-3} for natural-gas mole fractions well below 0.7. The reactions that drive molecular-weight–growth are substantially faster than those that will ultimately bring the system back to equilibrium.

Kinetic control is even more evident at 800 °C. Equilibrium predictions show that C_{5+} levels exceed 10^{-3} for natural-gas mole fractions greater than about 0.57. However it is evident from Fig. 8 (bottom panel) that significant C_{5+} is present at much lower natural-gas levels. For example, at residence times near 1000 s the kinetic predictions indicate natural-gas mole fractions as low as 0.3 produce C_{5+} levels above 10^{-3}. This is clear evidence of an equilibrium overshoot.

At 900 °C Fig. 18 shows that at equilibrium natural-gas mole fractions greater than about 0.46 are needed for C_{5+} to exceed 10^{-3}. The kinetics results are much different, as can be seen from Fig. 10. At 1000 s the C_{5+} level exceeds 10^{-3} for natural-gas mole fractions as low as 0.2.

Fig. 19 show the regions where C_{5+} levels exceed 10^{-3} as a function of temperature and initial natural gas in a natural-gas–steam mixture. The kinetics results at 600 and 700 °C (not presented in the paper) indicated very little reactivity in the system, thus the amount of C_{5+} is always well below 10^{-3}.

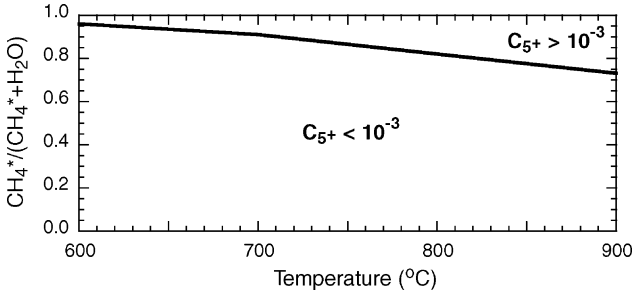

Fig. 19. Predictions of the natural-gas (CH_4^*) mole fraction (in a mixture of natural-gas and steam) at which the equilibrium C_{5+} exceeds 10^{-3} as a function of temperature.

However equilibrium predictions indicated that the amount of C_{5+} is greater than 10^{-3} for mole fractions of natural-gas greater than approximately 0.96 at 600 °C and 0.9 at 700 °C.

Fig. 19 shows that at 800 °C the equilibrium C_{5+} exceeds 10^{-3} only for natural-gas mole fraction greater than approximately 0.82. However the kinetics predictions in Fig. 12 show that at longer residence times the C_{5+} levels exceed 10^{-3} for all natural-gas mole fractions greater than approximately 0.1.

Equilibrium predictions at 900 °C show that C_{5+} levels exceed 10^{-3} for natural-gas mole fractions greater than about 0.73. However it is evident from kinetics predictions shown in Fig. 14 that C_{5+} exceeds 10^{-3} at residence times around 100 s for natural-gas mole fractions below around 0.1.

Generally speaking, under SOFC conditions the homogeneous chemistry is not in equilibrium. Even at times as long as 1000 s and temperatures as high as 900 °C, both major product species and C_{5+} levels are well out of equilibrium. In natural-gas–air mixtures the departure from equilibrium results from the dramatic decrease in conversion rates once oxygen is depleted. In natural-gas–steam mixtures the departure results from the very slow kinetics, resulting in slow conversion to equilibrium products. The molecular-weight–growth kinetics appear to be faster than the slow homogeneous "gasification" reactions for both natural-gas–air and steam mixtures. Thus for residence times of interest the kinetics predicts higher levels of C_{5+} than would be present at equilibrium.

5. Summary and conclusions

This paper reports a modeling investigation of the gas-phase reactions of methane and natural-gas mixed with either air or steam at temperatures from 600 to 900 °C and at a wide range of initial compositions and residence times relevant to SOFC operation. The results, presented as contour maps, provide a great deal of information summarizing the behavior of homogeneous chemistry as could occur in non-catalytic feed lines even before fuels enter the electrochemically active regions of the SOFC.

Adding even small amounts of air to methane or natural-gas significantly increases conversion to H_2, CO, H_2O, and CO_2. Under most circumstances oxygen is completely consumed within 10 s at 600 °C and within 1 s at 900 °C. Thus the fuel composition entering the active SOFC regions can be significantly different from the initial room-temperature mixture fed to the system. Such conversion can significantly affect the cell's electrochemical performance. For example, the steam that is formed homogeneously in the feed lines can participate immediately in reforming reactions on the SOFC anode, before any further H_2O is produced by charge-transfer chemistry.

Steam addition to the fuel mixture causes much less reaction than air addition. However at 900 °C and residence times above approximately 100 s there is significant conversion of the fuel to H_2 and higher hydrocarbons.

In addition to major gas-phase products, the model also predicts molecular-weight–growth to higher hydrocarbons. The sum of mole fractions of all species containing five or more carbon atoms, designated C_{5+}, is used as an indicator of deposit propensity via polyaromatic hydrocarbons. The methane–air mixtures generally produce much higher C_{5+} levels than the methane–steam mixtures at lower temperatures. However the C_{5+} levels in natural-gas–air mixtures is comparable to that in natural-gas–steam mixtures at higher temperatures. At 900 °C, C_{5+} mole fractions can exceed 10^{-3} at residence times greater that a few seconds. These C_{5+} levels raise a concern about deposit formation. Interestingly, the kinetic model predicts C_{5+} levels well above equilibrium levels for some residence times of interest.

As should be anticipated, higher temperatures lead to faster kinetics and natural-gas reacts more rapidly than methane. Nevertheless, the qualitative behaviors are similar. Some of the largest differences between methane and natural-gas are in the C_{5+} predictions, with natural-gas being more likely to form PAH deposits.

There are regions at longer residence times where the kinetics appears to be in steady state in the sense that species composition changes very slowly. However, by direct comparison with equilibrium predictions, the kinetics are found to be far from equilibrated. For the fuel–air cases the system appears to be kinetically "over-oxidized" in the sense that products like H_2O and CO_2 are greater than equilibrium values while H_2 and CO are lower. In the fuel–steam cases where the chemistry is very slow, the product species are predicted to be much lower the equilibrium values.

Acknowledgment

This work was supported by the DoD Multidisciplinary University Research Initiative (MURI) program administered by the Office of Naval Research under Grant N00014-02-1-0665.

References

[1] A. Weber, B. Sauer, A.C. Mller, D. Herbstritt, E. Ivers-Tiffe, Oxidation of H_2, CO and methane in SOFCs with Ni/YSZ-cermet anodes, Solid State Ionics 152/153 (2002) 543–550.
[2] E.P. Murray, T. Tsai, S.A. Barnett, A direct-methane fuel cell with a ceria-based anode, Nature 400 (1999) 649–651.
[3] G.J. Saunders, K. Kendall, Reactions of hydrocarbons in small tubular SOFCs, J. Power Sources 106 (2002) 258–263.
[4] H. Kim, S. Park, J.M. Vohs, R.J. Gorte, Direct oxidation of liquid fuels in a solid oxide fuel cell, J. Electrochem. Soc. 148 (2001) A693–A695.
[5] J.B. Wang, J.-C. Jang, T.-J. Huang, Study of Ni-samaria-doped ceria anode for direct oxidation of methane in solid oxide fuel cells, J. Power Sources 122 (2003) 122–131.
[6] J. Liu, S.A. Barnett, Operation of anode-supported solid oxide fuel cells on methane and natural gas, Solid State Ionics 158 (2003) 11–16.

[7] K. Kendall, C.M. Finnerty, G. Saunders, J.T. Chung, Effects of dilution on methane entering an SOFC anode, J. Power Sources 106 (2002) 323–327.
[8] S.J.A. Livermore, J.W. Cotton, R.M. Ormerod, Fuel reforming and electrical performance studies in intermediate temperature ceria-gadolinia-based SOFCs, J. Power Sources 86 (2000) 411–416.
[9] S. McIntosh, H. He, S.-I. Lee, O. Costa-Nunes, V.V. Krishnan, J.M. Vohs, R.J. Gorte, An examination of carbonaceous deposits in direct-utilization SOFC anodes, J. Electrochem. Soc. 151 (2004) A604–A608.
[10] Y. Jiang, A.V. Virkar, A high performance, anode-supported solid oxide fuel cell operating on direct alcohol, J. Electrochem. Soc. 148 (2001) A706–A709.
[11] Z. Zhan, J. Liu, S.A. Barnett, Operation of anode-supported solid oxide fuel cells on propane air fuel mixtures, Appl. Catal. A 262 (2004) 255–259.
[12] S.H. Clarke, A.L. Dicks, K. Pointon, T.A. Smith, A. Swann, Catalytic aspects of the steam reforming of hydrocarbons in internal reforming fuel cells, Catal. Today 38 (1997) 411–423.
[13] F.A. Coutelieris, S. Douvartzides, P. Tsiakaras, The importance of the fuel choice on the efficiency of a solid oxide fuel cell system, J. Power Sources 123 (2003) 200–205.
[14] C.Y. Sheng, A.M. Dean, The importance of gas-phase kinetics within the anode channel of a solid-oxide fuel cell, J. Phys. Chem. A 108 (2004) 3772–3783.
[15] R.J. Kee, M.E. Coltrin, P. Glarborg, Chemically Reacting Flow: Theory and Practice, John Wiley, 2003.
[16] P.N. Brown, G.D. Byrne, A.C. Hindmarsh, VODE: a variable coefficient ode solver, SIAM J. Sci. Stat. Comput. 10 (1989) 1038–1051.
[17] R.J. Kee, F.M. Rupley, E. Meeks, J.A. Miller, CHEMKIN-III: a FORTRAN chemical kinetics package for the analysis of gas-phase and plasma kinetics, Technical Report SAND96-8216, Sandia National Laboratories, 1996.
[18] M. Frenklach, J. Warnatz, Detailed modeling of PAH profiles in a sooting low-pressure acetylene flame, Combust. Sci. Tech. 51 (1987) 265–283.
[19] K. Roy, M. Braun-Unkhoff, P. Frank, T. Just, Kinetics of the cyclopentadiene decay and the recombination of cyclopentadienyl radicals with H-atoms: enthalpy of formation of the cyclopentadienyl radical, Int. J. Chem. Kin. 33 (2001) 821–833.
[20] C. Naik, Modeling the low to intermediate temperature oxidation of hydrocarbons, Ph.D. Thesis, Colorado School of Mines, 2005.
[21] G.P. Smith, D.M. Golden, M. Frenklach, N.W. Moriarty, B. Eiteneer, M. Goldenberg, C.T. Bowman, R.K. Hanson, S. Song, W.C. Gardiner, V. Lissianski, Z. Qin, GRI-Mech—an optimized detailed chemical reaction mechanism for methane combustion, Technical Report, Gas Research Institute, 1999. http://www.me.berkeley.edu/gri_mech.
[22] C.J. Chen, M.H. Back, R.A. Back, The thermal decomposition of methane. II. Secondary reactions, autocatalysis and carbon formation; non-arrhenius behaviour in the reaction of CH_3 with ethane, Can. J. Chem. 54 (1976) 3175–3184.
[23] M.H. Back, R.A. Back, Pyrolysis: Theory and Industrial Practice, Academic Press, 1983.
[24] A. El Bakali, P. Dagaut, L. Piller, P. Desgroux, J.-F. Pauwels, A. Rida, P. Meunier, Experimental and modeling study of the oxidation of natural gas in a premixed flame, shock tube, and jet stirred reactor, Combust. Flame 137 (2004) 109–128.